Selective energy filtering in a multiple-quantum-well nanodevice: The quantum cascade cooler

Guéric Etesse, Chloé Salhani, Xiangyu Zhu, Nicolas Cavassilas, Kazuhiko Hirakawa, Marc Bescond

Selective energy filtering in multiple quantum well nanodevice : The Quantum Cascade Cooler

Guéric Etesse,[1,*] Chloé Salhani,[2,3] Xiangyu Zhu,[2] Nicolas Cavassilas,[1] Kazuhiko Hirakawa,[2,3] and Marc Bescond[1,2,†]

[1] *IM2NP, UMR CNRS 7334, Aix-Marseille Université, Technopôle de Château-Gombert, Bâtiment Néel, 60 Rue Frédéric Joliot Curie, 13453 Marseille, France*

[2] *Institute of Industrial Science, University of Tokyo, 4-6-1 Komaba, Meguro-ku, Tokyo 153-8505, Japan*

[3] *LIMMS-CNRS, IRL 2820, 4-6-1 Komaba, Meguro-ku, Tokyo 153-8505, Japan*

Abstract

Using quantum transport simulations, we study the operating principle of a proposed Quantum Cascade Cooler, a multiple quantum well structure whose cooling capabilities rely on combined resonant tunneling and thermionic emission filtering. We couple charge and heat transport by self-consistently solving non-equilibrium Green's functions and heat equation, and subsequently calculate thermodynamic properties of the electrons using non-invasive virtual probes. We show that such device exhibits bias dependent electron temperature oscillations emerging from electron-phonon interactions and inter-subband transitions. Finally, we show the advantage of a multiple quantum well structure over a single quantum well one and discuss the actual potential for such structure to effectively cool down the crystal lattice upon optimization.

I. INTRODUCTION

In the last few decades, the need for improved heat management devices and systems has become a major challenge for energetic and environmental purposes, as well as to avoid technical limitations on state-of-the-art electronic devices.

For instance, amongst the so-called Information Communication Technology (ICT) sector, the increasing demand for data centers resulted in a consumption estimated to 1.4 percent of the total, worldwide, energy consumption from which almost half of the amount had been used solely for cooling purposes [1, 2]. The carbon footprint of such facilities is estimated to undergo the highest growth rate across the whole ICT sector [3], the latter being responsible for 2 percent of CO_2 emissions, a proportion comparable to the aviation sector [3].

Besides, modern microchips have continued to follow Moore's Law stating that transistor count is doubling every two years [4–6] and have now attained transistor densities of the order of the billion devices per chip. Power densities associated are hence dangerously approaching values hard to administer without substantial enhancement for the cooling processes, leading to the apparition of software limitations on the clock speed in some recent processors [4, 7].

Current active heat dissipation methods, including fanning or liquid cooling, have the advantage of large coefficients of performance [8]. They however lack the compactness and

* gueric.etesse@im2np.fr

† bescond@iis.u-tokyo.ac.jp

silence required for portable devices [9]. More importantly, the apparition of hot spots due to the miniaturization of electronic devices down to sizes comparable with the phonon mean free path [10–12] cannot be properly addressed by these type of approaches. Indeed, they resort on the extraction of heat diffused to a heat sink and therefore cannot deal with the non-uniformity of temperature emerging with localized hot spots.

Thermoelectric refrigeration systems using Peltier effect [13] have been investigated as a possible solution to address those hot spots. Their size, of a few hundred microns, however induces significant amount of scattering processes amongst the electrons, which in turn leads to a reduced power factor $S^2\sigma$ where S is the Seebeck coefficient and σ is the electrical conductivity. An approach overpassing these scattering issues, could be the thermionic refrigeration [14]. Within this approach, electrons absorb heat from the cathode [15] and are thermionically transmitted to the anode before scattering processes can take place. It has also been observed that, with such mechanism, it was possible for a semiconductor heterostructure at room temperature to directly cool down the electrons before they transfer energy to the lattice [16].

An asymmetric double barrier heterostructure, originally proposed by Chao et al. [17], takes advantage of resonant tunneling across a first thin barrier and restrict the injection to cold electrons. It has been shown by Yangui et al. that the thermionic emission from the quantum well (QW) led to substantial evaporative cooling of the electrons up to 50 K below room temperature [16]. In the present work, we propose and theoretically investigate an $AlGaAs$ based heterostructure, shown in Figure 1, derived from the asymmetric double barrier, and consisting of sequentially stacked QWs. Thanks to appropriate band engineering, it is possible to progressively increase the energy level of successive QW state. In this configuration, an electron absorbing a phonon in the first QW can tunnel into the next QW of the structure, where another phonon can be absorbed. Electrons are finally extracted from the last QW by thermionic emission over a thicker layer, acting as a thermal wall to prevent heat backflow. This process is similar to the one occurring in quantum cascade laser [18] between electron and photon emission, which leads us to identify this structure as "Quantum Cascade Cooler" (QCC). The role of the successive barriers is to filter injected electrons and to concentrate the cooling in the QWs. By doing so, we will be able to precisely refrigerate nanoscale regions and to demonstrate a proof of concept to answer the hot spots issue. This type of solution will require to be

adapted to the specifics of the device it aims to cool, depending on the materials and the type of circuit conception. The exact general application of those nanocoolers is however out of the scope of the present article.

Using quantum transport code based on the non-equilibrium Green's functions (NEGF) formalism coupled to the heat equation, we show that electron temperature in each QW depicts anti-correlated oscillations as a function of the applied voltage. Simulations show that those temperature oscillations depend on the energy difference between two consecutive QW states and are directly linked to the polar optical phonon energy. The paper is organized as follows. Section II presents the theoretical framework used to compute electron and heat transport as well as the local thermodynamic properties of the electrons. Section III develops the physical analysis associated to the studied structure. Section IV finally concludes this work by summarizing the key findigs.

II. THEORETICAL APPROACH

We consider the heterostructure represented in Figure 1 whose emitter (cathode) and collector (anode) regions are n-doped $GaAs$ layers with a donor concentration of 10^{18} cm^{-3}. The undoped active region is composed of five layers: we consider two 5 nm thick QWs composed of $Al_{0.1}Ga_{0.9}As$ and $Al_{0.2}Ga_{0.8}As$ labeled as QW1 and QW2, respectively. QW1 is separated from the emitter and QW2 by 6 nm thick $Al_{0.35}Ga_{0.65}As$ barriers. Finally, QW2 is separated from the collector by a 30 nm $Al_{0.35}Ga_{0.65}As$ barrier.

Applying a voltage bias between the two contacts induces a non-equilibrium transport regime of carrier which typically results in two different temperatures for the lattice and electrons. Indeed, such a transport being filtered in energy thanks to the tunnelling and thermionic process, it leads to a temperature of electrons controlled by evaporative cooling effect [16] while lattice temperature is controlled by transfer of energy from the lattice to the electron bath through electron-phonon scattering [15].

The theoretical study of such physical processes for a realistic device requires to consider both electron and phonon transport. In order to do so, we use an in-house code in which electron and heat transport are solved self-consistently. We subsequently use virtual Büttiker probes to unambiguously determine the local electronic temperature and electrochemical potential inside the device.

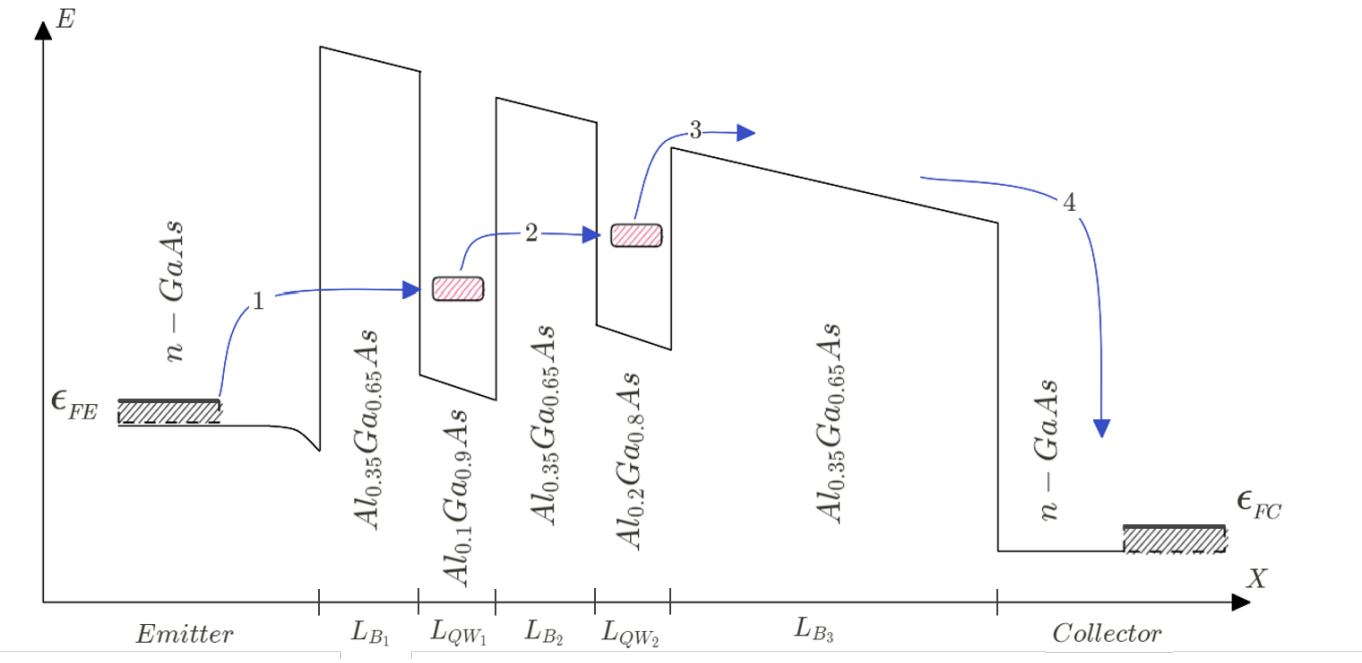

FIG. 1: Considered Quantum Cascade Cooler with $L_{B_1} = L_{B_2} = 6$ nm, $L_{QW_1} = L_{QW_2} = 5$ nm and $L_{B_3} = 30$ nm. The solid black line corresponds to the edge of the conduction band. ϵ_{FE} and ϵ_{FC} are the Fermi levels of the emitter and collector respectively. The ground states of the quantum wells are described by the red dashed rounded rectangles. The intended working principle is represented by the successive blue arrows and decomposed in 4 steps. (1) The electrons are injected from the emitter in the first quantum well (QW1) by resonant tunneling. (2) Electrons are injected in the second quantum well (QW2) by phonon assisted tunneling. (3) Electrons are thermionically extracted from the second quantum well. (4) Electrons are progressively relaxed in the collector through electron-phonon interactions.

A. Electron transport model

The description of the method used to calculate electron and heat transport for this work has been thoroughly presented in previous work [19]. Equations required for the analysis presented in this work will nonetheless be recalled.

Let us first introduce the retarded Green's function at energy E and transverse wavevector k_t.

$$G^r_{k_t} = [(E-V)I - H_{k_t} - \Sigma^r_{L,k_t} - \Sigma^r_{R,k_t} - \Sigma^r_{S,k_t}]^{-1}, \tag{1}$$

where V is the electrostatic potential energy, considered only transport axis dependant and thus invariant in the transverse plan, I is the identity matrix, $H_{k_t}$is the effective mass Hamiltonian describing the Γ valley of the conduction band, $k_t = n_{k_t} \times 2\pi/L_t$ is the transverse wavevector with n_{k_t} an integer and L_t the perpendicular dimension of the system. $\Sigma^r_{L(R),k_t}$ are the self-energies for the left (L) and right (R) semi-infinite device contacts, Σ^r_{S,k_t} is the self-energy calculated within the self-consistent Born approximation (SCBA) that accounts for the interaction between electrons and both the acoustic phonons and polar optical phonons. In our approach, acoustic and polar-optical phonon baths are considered at equilibrium and locally follow a Bose-Einstein distribution. They are however, not in equilibrium with one another. We thus need to define two different temperatures T_{AC} and T_{OP}, the temperature of acoustic and polar optical phonons, respectively. The physical reason for this is the unbalance in their respective energy densities leading to the net anharmonic decay of optical phonons into acoustic ones which has a critical impact on the thermal transport[20]. These temperatures are self-consistently computed by coupling the electron transport equations with the heat equation as presented in subsection II B.

The lesser/greater Green's functions are obtained by deriving the retarded Green's functions using the following identities:

$$G^{\lessgtr}_{k_t} = G^r_{k_t}(\Sigma^{\lessgtr}_{L,k_t} + \Sigma^{\lessgtr}_{R,k_t} + \Sigma^{\lessgtr}_{S,k_t})G^{r\dagger}_{k_t}, \tag{2}$$

$$\Sigma^r = \frac{1}{2}[\Sigma^> - \Sigma^<], \tag{3}$$

where the total scattering self-energy, for a given mode k_t, can be decomposed into

$$\Sigma^{\lessgtr}_{S,k_t} = \Sigma^{\lessgtr}_{AC,k_t} + \Sigma^{\lessgtr}_{POP,k_t}, \tag{4}$$

where $\Sigma^{\lessgtr}_{AC,k_t}$ is the self-energy for acoustic phonons calculated within the elastic assumption at position j along the transport axis that can be expressed as [21, 22]

$$\Sigma^{\lessgtr}_{AC}(j,j;E) = \sum_{k'_t} \pi(2n_{k'_t}+1)\frac{\Xi^2 k_B T_{AC}(j)}{\rho u_s^2}(j) G^{\lessgtr}_{k'_t}(j,j;E), \tag{5}$$

where Ξ is the deformation potential, ρ is the mass density, u_s is the sound velocity and T_{AC} is the temperature of acoustic phonons. We assume interactions with acoustic phonons to be local and therefore only consider the diagonal part of the Green's function [23].

The scattering self-energy for polar optical-phonons is defined in Eq. 6 and we use the diagonal expression that have been proposed in previous work by Moussavou et al. to effectively describe their long range interactions [24]. For a given wavevector k_t, we have :

$$\Sigma^{\lessgtr}_{POP,k_t}(j,j;E) = \frac{\lambda M^2}{2\pi S}\sum_{k'_t}[(n_L(j)+1)G^{\lessgtr}_{k'_t}(j,j;E\pm\hbar\omega_{LO}) + (n_L(j))G^{\lessgtr}_{k'_t}(j,j;E\mp\hbar\omega_{LO}))]$$

$$\times\int_{\pi/L_t}^{\pi}\frac{\pi(2n_{k'_t}+1)}{\sqrt{(k_t-k'_t cos\theta)^2+(k'_t sin\theta)^2}}d\theta, \tag{6}$$

where $n_L(j) = (e^{(\hbar\omega_{LO})/(k_B T_{POP})}-1)^{-1}$ with $\hbar\omega_{LO}$ the LO phonon energy and T_{POP} their temperature, M is the Fröhlich factor, θ is the angle between k_t and k'_t. λ is a scaling factor correcting for the reduced strength emerging from the diagonal approximation. The value $\lambda = 8$ used in this paper has been obtained using the physically-based analytical model developed in Ref. [24].

Once the Green's functions are obtained we have access to all the physical properties of interest.

The electron density n_j at position j along the transport axis is given by:

$$n_j = -2\times\frac{i}{2\pi}\int G^{<}_{j,j}(E)dE, \tag{7}$$

with $G^{<}_{j,j}(E) = \sum_{k_t}\pi(2n_{k_t}+1)G^{<}_{k_t,j,j}(E)$

The electron current density (in A/m^2), $J_{j\to j+1}$ from position j to $j+1$:

$$J_{j\to j+1} = \int \mathcal{J}_{j\to j+1}(E)dE, \tag{8}$$

where $\mathcal{J}_{j\to j+1}(E)$ is the electron current density spectrum (in A/(m^2.eV)):

$$\mathcal{J}_{j\to j+1}(E) = \frac{e}{\hbar}\sum_{k_t}\frac{2n_{k_t}+1}{S}[H_{j,j+1}G^{<}_{k_t,j+1,j}(E) - G^{<}_{k_t,j,j+1}(E)H_{j+1,j}]. \tag{9}$$

We can then deduce the electronic energy current that reads:

$$J^E_{j\to j+1} = \int\frac{E}{e}\mathcal{J}_{j\to j+1}(E)dE, \tag{10}$$

whose first derivative of the electronic energy current corresponds to the cooling power density (in W/m^3):

$$Q_j = -\nabla_j\cdot J^E. \tag{11}$$

Q_j being the source term allowing to couple the electron transport equation to the heat equation. A negative value of Q_j corresponds to an increase of the electronic energy current density and then to a transfer of energy from the lattice to the electronic bath, leading to a cooling of the lattice. A positive value corresponds to the opposite phenomenon, i.e. the heating of the lattice.

B. Heat transport model

The lattice temperature is computed by solving the 1D heat equation along the direction of transport. The discretized heat equation at site j can be expressed as:

$$\left[-\frac{\partial}{\partial x}[\kappa_{th}(x)\frac{\partial}{\partial x}T_{AC}(x)]\right]_j = Q_j, \tag{12}$$

The thermal conductivity of the material κ_{th} is taken equal to 4 W/(m·K) in the QWs region in order to take into account the increased thermal resistance emerging from the interface between layers[25, 26]. In the rest of the device it is set to the bulk value of GaAs (46 W/(m·K)). The temperature considered in the heat equation T_{AC} is the temperature of acoustic phonons. They have a larger velocity than their optical counterpart and are therefore mainly responsible of heat transport[27]. Left and right contact temperatures are set to $T_{AC} = 300$ K by enforcing Dirichlet boundary conditions. This assumption corresponds to consider massive contacts with a sufficiently high thermal capacitance. Q_j is the cooling power density (CPD) previously defined (See Eq.11) which ensures local energy conservation between electron and phonon systems. From a physical point of view, since the acoustic phonons have a much lower energy than the energy range of interest, their interactions with electrons is assumed to be elastic. This implies that electrons loose or increase their energy by scattering with polar optical-phonons. In turn, optical phonons decay into acoustic phonon modes, which sustains the thermal energy propagation along the device. In stationary conditions, the power transfer from optical to acoustic phonons must be equal to the cooling power density Q_j. Within a relaxation time approximation, we can thus write

$$\frac{(T_{POP}(j) - T_{AC}(j))C_{POP}}{\tau_{POP\rightarrow AC}} = Q_j, \tag{13}$$

where $\tau_{POP\rightarrow AC}$ is the relaxation time of polar optical phonons into acoustic phonons ($\tau_{POP\rightarrow AC} = 4.16\times10^{-12}$ s) and C_{POP} is the thermal capacitance of polar optical phonons per unit volume ($C_{POP} = 1.72\times10^{6}$ J/(m^3·K)). The numerator of the left side expresses the average energy per unit volume exchanged between the polar optical and acoustic phonon baths in an interval $\tau_{POP\rightarrow AC}$. Eq. 13 allows us to compute $T_{POP}(j)$ from the knowledge of Q_j and $T_{AC}(j)$. The computed values of T_{AC} and T_{POP} are substituted in Eq. 5-6. This establishes the coupling between the heat equation and the electron transport equations. The heat equation is iteratively solved together with the transport equations and the Poisson equation, until the criteria of convergence for both electron density and carrier current density are reached. The potential energy V is self-consistently determined by nonlinearly coupling the transport equations with the Poisson equation through the electron density.

C. Local electron temperature

As a post processing step, we use the virtual Büttiker probe [28, 29] to calculate local electron temperature. It is based on the introduction of a local non invasive probe defined at position j by its self-energy:

$$\Sigma^{>}(j,j;E) = -i[1 - f_{FD}(E,\mu_j,T_j)] \times i[\frac{G^{>}(j,j;E) - G^{<}(j,j;E)}{2\pi}] \times \nu_{coup} \tag{14}$$

$$\Sigma^{<}(j,j;E) = i f_{FD}(E,\mu_j,T_j) \times i[\frac{G^{>}(j,j;E) - G^{<}(j,j;E)}{2\pi}] \times \nu_{coup} \tag{15}$$

where $f_{FD}(E,\mu_j,T_j)$ is the Fermi-Dirac distribution of the probe depending on the electrochemical potential μ_j and the electronic temperature T_j. $i[\frac{G^{>}_{j,j}(E)-G^{<}_{j,j}(E)}{2\pi}]$ is the local density of states, common to the probe and the device.

Using the previously determined Green's functions of the device, we calculate the electrons and energy currents between the probe and the device.

$$(\Delta I_e)_j \equiv \int_0^{\infty} [\Sigma^{>}_{j,j}(E)G^{<}_{j,j}(E) - G^{>}_{j,j}(E)\Sigma^{<}_{j,j}(E)]dE \tag{16}$$

$$(\Delta I_q)_j \equiv \int_0^{\infty} \frac{E}{e}[\Sigma^{>}_{j,j}(E)G^{<}_{j,j}(E) - G^{>}_{j,j}(E)\Sigma^{<}_{j,j}(E)]dE \tag{17}$$

The principle is now to find $[T_j;\mu_j]$ such that $(\Delta I_e)_j$ and $(\Delta I_q)_j$ vanish. The probe is then in a local equilibrium with the device, itself arbitrarily out-of-equilibrium. The

temperature and chemical potential of the probe are therefore accurate measurements of the device thermodynamic properties.

In order to find the vanishing conditions of the currents in each point of the device, we solve the two coupled non-linear equations (16) and (17) using a Newton-Raphson algorithm.

This method determines the electronic temperature and electrochemical potential in systems arbitrarily far from equilibrium provided the probe is localized, weak and broadband, to ensure that the properties of the device are measured while avoiding perturbation by the probe [28]. These conditions being satisfied by the proposed probe, it is expected to yield a unique and an unambiguous electronic temperature and chemical potential. In the following section, we will restrict ourselves to the study of the electronic temperature based on this approach.

III. RESULTS AND DISCUSSION

In this section we analyze the physical properties of the Quantum Cascade Cooler whose local density of state and potential profile are represented in Figure 2-a). We clearly see that the structure parameters taken in Figure 1 lead to the desired step-like feature of the QW states. We also compare its properties with those of the SQW structure whose local density of state and potential profile are represented in Figure 2-b)

A. Electron temperatures

In this section we explain the electronic temperature behaviours in each quantum well for the structure Figure 3 first shows the electron temperatures in QW1 and QW2 as a function of the applied bias. We observe a phase opposition of oscillations between those two temperatures. Figure 3 also shows W, the energy difference between the two QW ground states. We see that the period of oscillations corresponds to polar optical phonon energy $\hbar\omega_{LO}$, equal to 35 meV [30]. In order to explain those dependencies we analyze the injected and extracted current spectra impacting the electron distributions in each QW.

The first extrema of electron temperatures, at $V = 0.175$ V, corresponds to $W \approx \hbar\omega_{LO}$. At this bias, Figure 4-a) shows that the current density spectra (see Eq. 9) from the emitter to QW1, and from QW1 to QW2 exhibit maxima that are separated by the polar optical

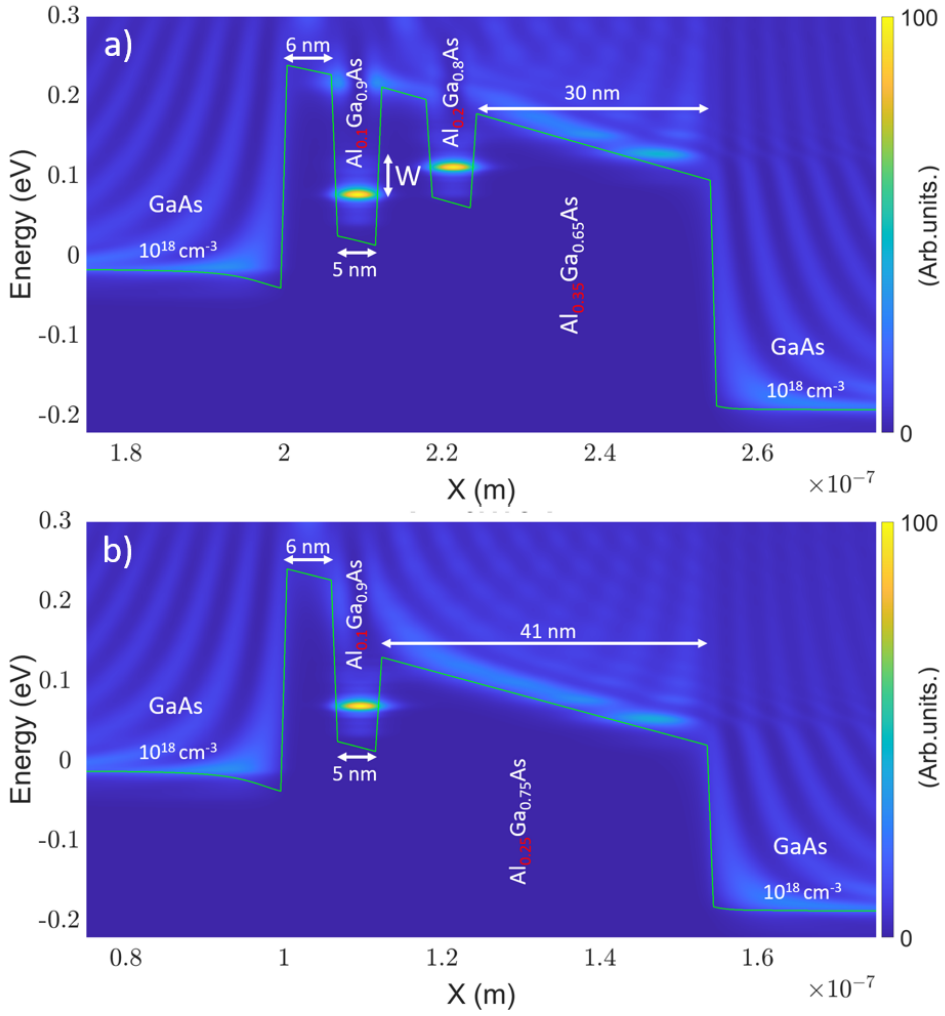

FIG. 2: Local density of states (colormap) and potential profile (green solid line) of the (a) SQW and (b) QCC for a voltage bias of $V = 0.175$ V. QCC is obtained from the parameters of Figure 1. The 0 of energy is set to the emitter Fermi energy.

phonon energy $\hbar\omega_{LO}$. Moreover, in Figure 4-b) representing the first subband of the two QWs, we can see that the energy difference between the ground states of the two QWs is also equal to $\hbar\omega_{LO}$. This ensures that the intersubband transition between the two ground states is principally controlled by LO phonon absorption. Indeed, since $W > k_bT \approx 25$ meV, most thermally excited electrons cannot directly tunnel from QW1 to QW2 through elastic scattering processes. Due to the broad injection coming from the emitter alongside with the lack of selective extraction of thermally excited electrons, the distribution of electrons in

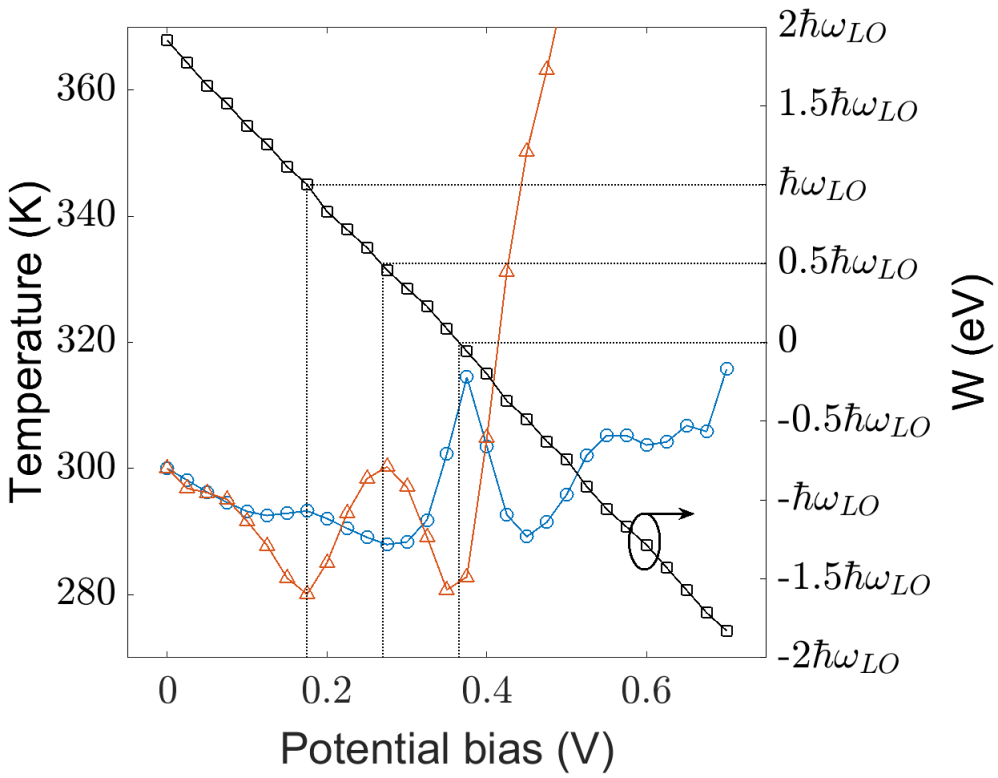

FIG. 3: Representation of the calculated electronic properties as a function of bias. Average temperature of the electrons in the first (blue line with circle markers) and second QW (orange line with triangle markers); W, the energy difference between the first and second QW's ground state (black line with square markers).

QW1 becomes hotter. Conversely, due to the effective injection of electrons assisted by LO phonon absorption near the ground state of QW2, followed by the thermionic extraction of electrons above the last thick AlGaAs barrier, the distribution of electrons in QW2 becomes colder. As a result, in Figure 4-c) which shows the electron density spectrum in the QWs, QW1 (QW2) exhibits a broader (narrower) distribution, consistent with a higher (lower) electron temperature.

At $V = 0.275$ V, the energy difference between the two subbands is $W \approx \frac{1}{2}\hbar\omega_{LO}$. We can see on Figure 5-a), which shows electron current density spectra for both QWs, that the maximum of injection in QW2 now happens $\frac{1}{2}\hbar\omega_{LO}$ above QW2 ground state. Although the absorption of one LO phonon by electrons in QW1 can only lead to this energy or

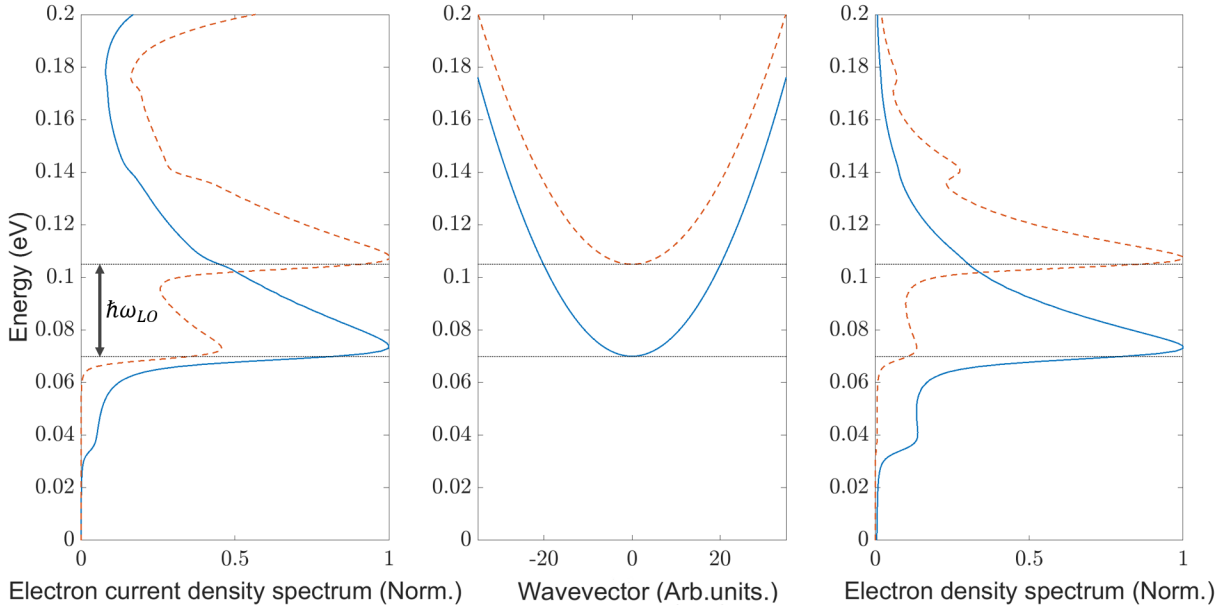

FIG. 4: $V = 0.175$ V. a) Normalized electron current density spectrum in the first QW (blue solid line) and between both QWs (orange dashed line); b) First subband for the first (blue solid line) and second QW (orange dashed line) represented as a function of the transverse wavevector, k_t; c) Electron density spectrum for the first (blue solid line) and second QW (orange dashed line). In all sub-figures, ground states of the first subbands of both QW are also represented (horizontal dotted lines) across each tile.

higher, the presence of a peak at QW2 ground state's energy demonstrates that an other scattering mechanism occurs. Figure 5-b) shows the first subband of the two QWs. Here, we can see that since W is equal to $\frac{1}{2}\hbar\omega_{LO}$, the minimum change in wavevector required for the intersubband transition assisted by LO phonons is non zero. Due to the wavevector dependancy in the polar optical phonon self-energy (See Eq. 6), the LO phonon absorption is thus less efficient than in the previous case (i.e $V = 0.175$ V). Moreover the value of W is now inferior to k_bT, leading to a substantial component of the thermally excited electrons which can tunnel through elastic scattering with acoustic phonons. This possible extraction of thermally excited electrons via elastic scattering processes thus induces a local minimum of electron temperature in QW1. Finally, in Figure 5-c), which represents the electron density spectra in QW1 and QW2, we can see that the electron density spectrum

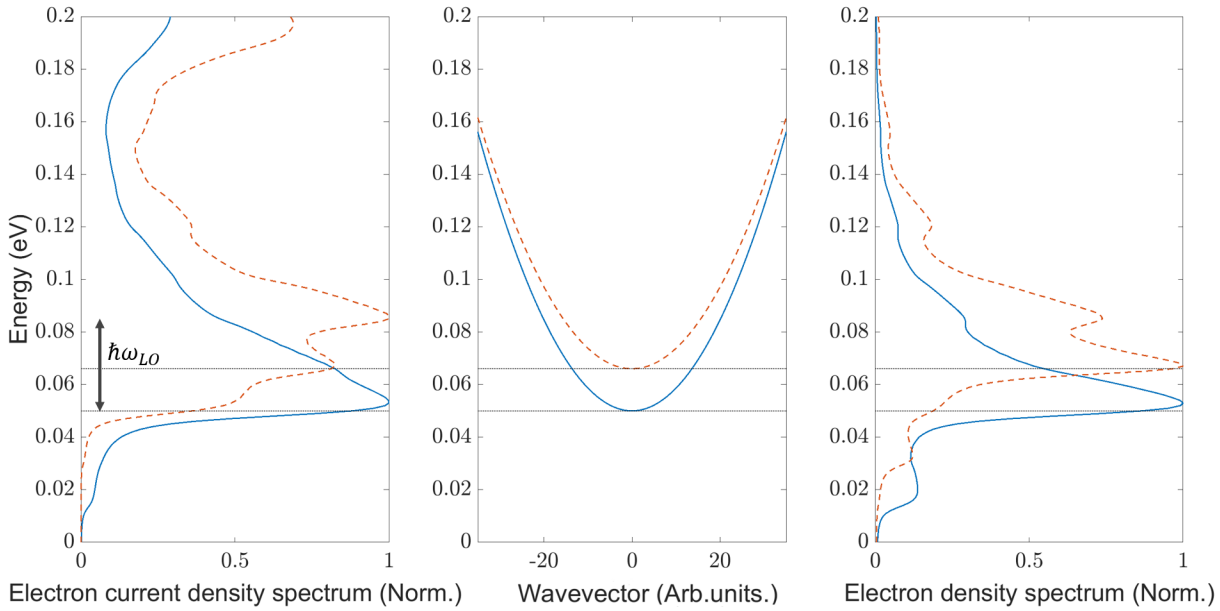

FIG. 5: Same as figure 4 for $V = 0.275$ V.

in QW2 exhibits two peaks. One is located near QW2 ground state, and the other is $\frac{1}{2}\hbar\omega_{LO}$ above QW2 ground state, corresponding to the energy of the shifted maximum of current. This evidences that the energy selective injection resulting from electron-phonon interaction shapes the electron distribution and thus the electron temperature. The injection of electrons in QW2 at this energy resulting from LO phonon absorption thus leads to a local maximum of electron temperature in QW2.

Finally at $V = 0.375$ V, $W \approx 0$, which is the resonant case where the QW ground states are aligned. Unlike for the two previous biases, electrons near QW1 ground state energy do not need to absorb phonons to flow from QW1 to QW2. In Figure 6-a), representing the electron current density spectra from the emitter to QW1 and from QW1 to QW2, we can see that the current density spectrum gets narrower between the injection in QW1 and the injection in QW2. This narrowed injection stems from the fact that electrons in QW1 which are 35 meV above the ground state can now emit LO phonons to get injected in QW2. However, as it can be seen on Figure 6-b), which represents the first subband of the two QWs, electrons of QW1 below this energy are forbidden to emit LO phonons as this would result in an injection below QW2 ground state. In Figure 6-c) representing the

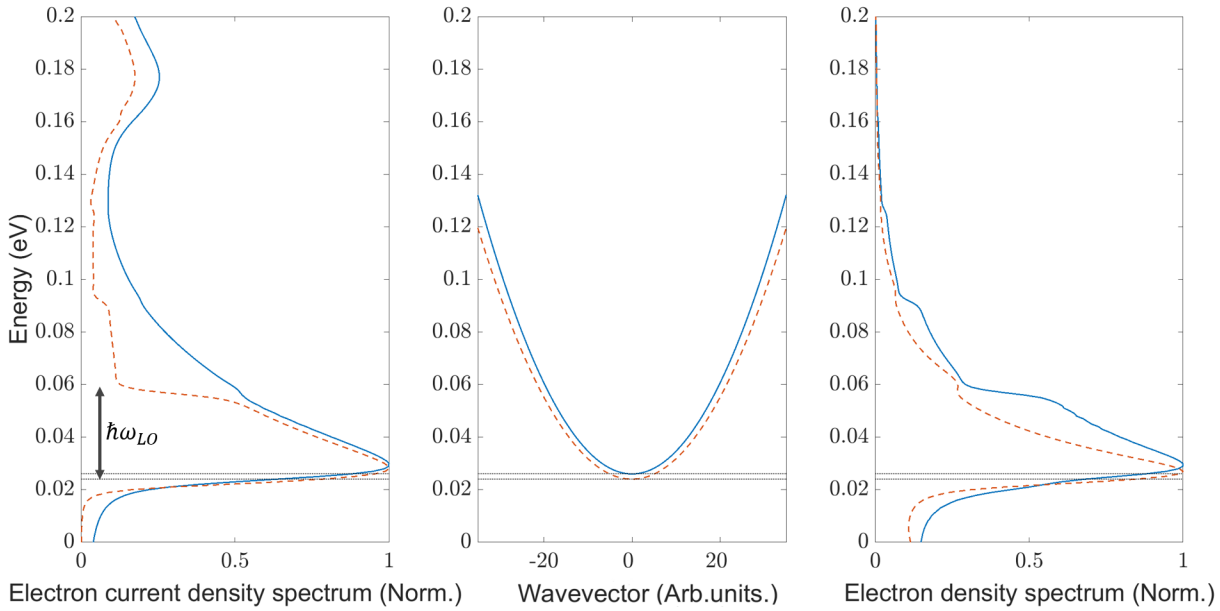

FIG. 6: a) Same as figure 4 and figure 5 for $V = 0.375$ V.

electron density spectra in both QWs, we can see that this narrow energy range acts as a bottleneck for electrons in QW1 and leads to the apparition of a shoulder at 0.055 eV. This is consistent with the fact that this configuration corresponds to a maximum of temperature for electrons in QW1. Conversely, the narrow injection in QW2 alongside with the subsequent thermionic emission above the last thick AlGaAs barrier leads to a distribution of electrons corresponding to a lower temperature.

Above $V = 0.375$ V, in Figure.4, we observe a fast increase of the temperature in QW2. Since W becomes negative, electrons are injected in QW2 at energies above ground state. On the other hand, electron temperature in QW1 remains closer to 300 K until a bias of 0.65 V is reached, for which QW1's ground state becomes lower than the emitter conduction band edge, where the same phenomenon happens.

B. Cooling properties

In this section we compare the cooling properties of the present Quantum Cascade Cooler to its single quantum well (SQW) counterpart. In order to faithfully compare the two

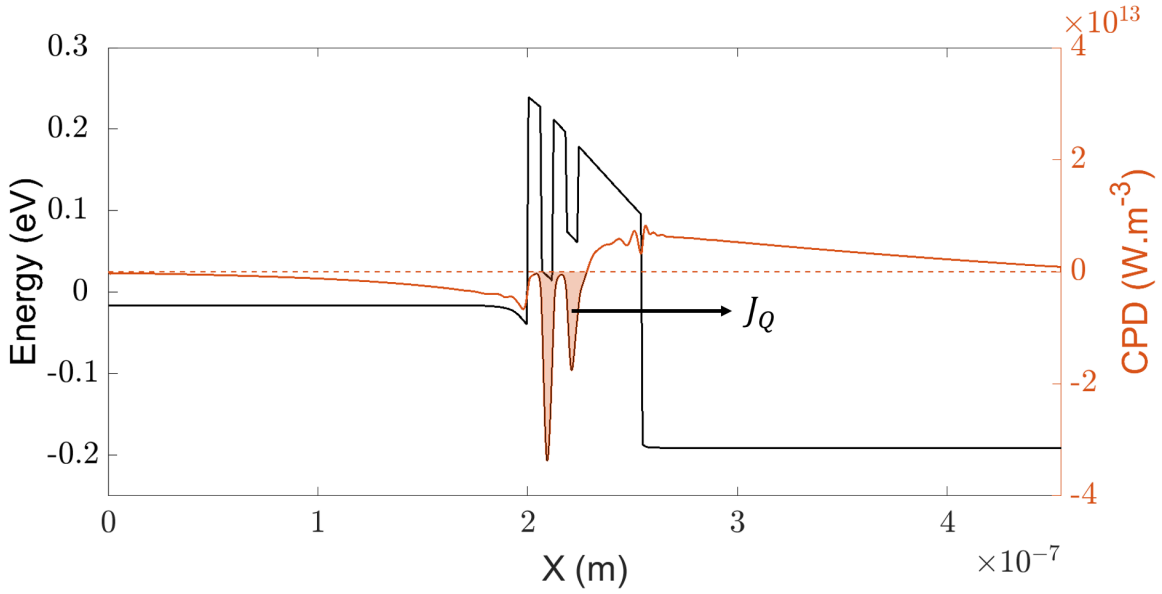

FIG. 7: Potential profile (black line) and cooling power density Q_j(orange solid line), for a voltage bias of V =0.175 V. The base line (orange dashed lined) and the cooling power (orange area), J_Q, are also represented. The 0 of energy is set to the emitter Fermi energy.

structures, we consider a SQW device of same length where the energy gap between the emitter Fermi level and the first QW state is conserved at equilibrium. Moreover, the energy interval between the QW level and the top of the second barrier is taken identical to the the one between the level of the second QW and the last barrier of the QCC. In order to do so, we replace the second barrier, the second quantum well, and the last barrier of the QCC by a 41nm single barrier of $Al_{0.25}Ga_{0.75}As$. The new structure's local density of states and potential profile are represented in Figure 2-b) for a bias of $V = 0.175$ V.

By integrating the negative part of the cooling power density Q_j (See Eq. 11) over x (the direction of transport) as represented by the orange area in Figure 7, we obtain the cooling power (J_Q) of the central region (between the middle of the first barrier and the end of last barrier). This quantity is represented for both devices in Figure 8-a). We also represent the contribution of QW1 and QW2 to the cooling power for the QCC. This cooling power is obtained by integrating the negative part of the cooling power density Q_j (See Eq. 11) over x (the direction of transport) as represented in Figure 7. Of course, integrating both the negative and positive components of Q_j over the whole device systematically yields a positive value equal to the supplied electrical power ($P_{Supplied} = J \times V$). This corresponds to an overall heating of the device. We are studying the cooling of the QW region of the

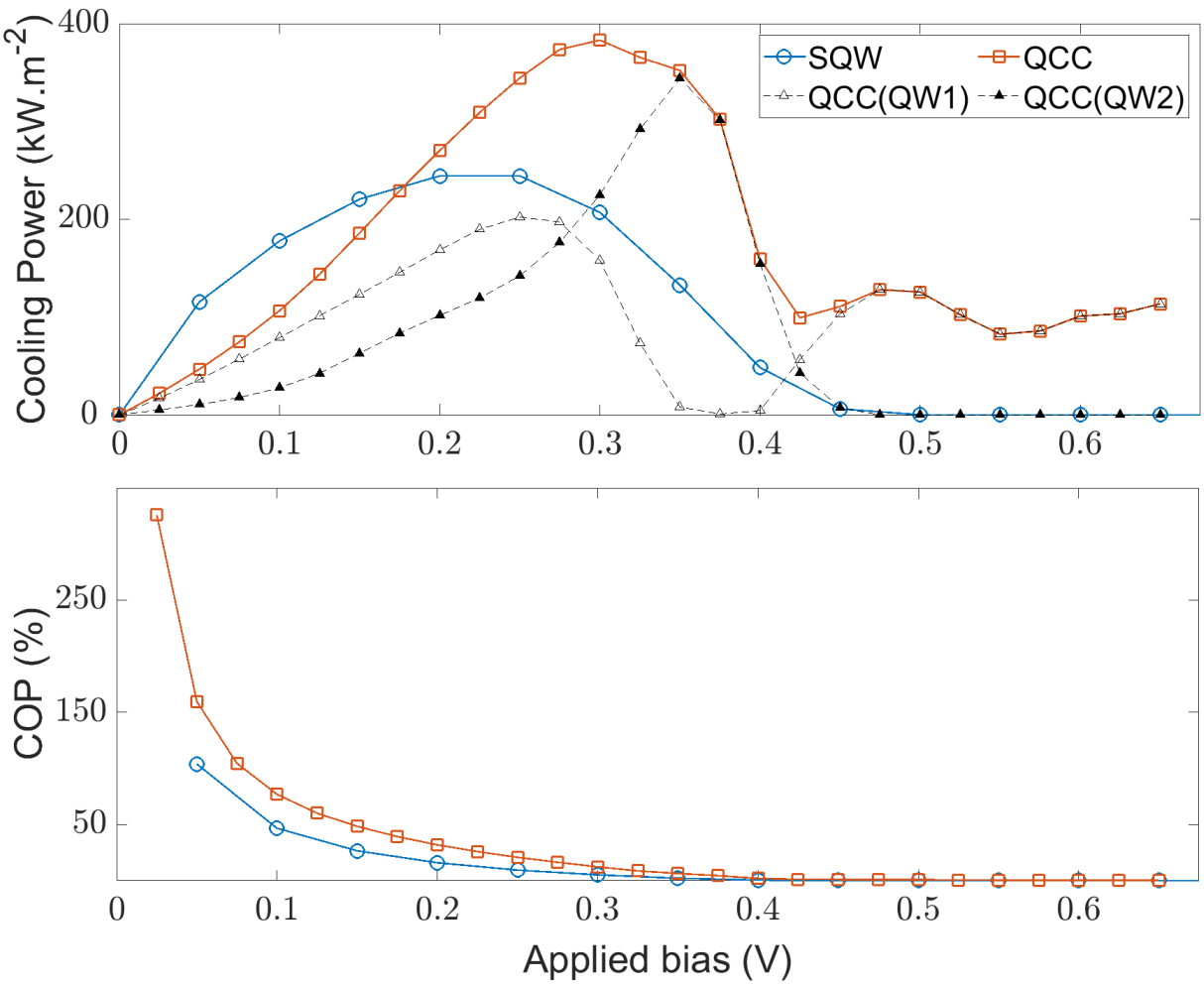

FIG. 8: a) Cooling power, (J_Q), as a function of potential bias for the SQW (blue line with cricle markers) and the QCC (orange line with square markers). Contribution of QW1 and QW2 to the cooling power are also represented (black dashed lines with hollow and filled triangle markers, respectively) b) Coefficient of performance (COP) as a function of the potential bias for the SQW (blue line with circle markers) and the QCC (orange line with square markers).

device, we therefore restrict ourselves to the calculation of the heat transferred in its central region.

We can first see that the QCC yields lower cooling powers than the SQW structure for biases below $V = 0.175$ V. However, its maximum cooling power is much greater. Indeed, $J_Q = 383$ kW/m^{-2} at $V = 0.3$ V for the QCC whereas the maximum is only of 244 kW/m^{-2} at $V = 0.25$ V for the SQW. Similarily to the temperature of the electrons, the QCC cooling

power depicts oscillations. Such oscillations take their origins in the phenomena described in the previous section. This can be directly deduced from QW1's and QW2's contribution to the QCC cooling power, which are locally maximized at biases corresponding to local minima of electronic temperature (see Figure 3). The overall maximum cooling power is obtained for $W \approx 0.5\hbar\omega_{LO}$ where both QWs contribute to the cooling.

Figure 8-b) shows the corresponding coefficient of performance (COP), which is defined as the ratio between J_Q over $P_{Supplied}$. For both structures, the COP decreases with the bias as it is unfortunately usual in thermionic cooling devices (see Figure 4 in Ref.[31]). However, for all biases the COP of the QCC is significantly higher than the COP of the SQW structure. This result shows that for the same flux of electron, more phonons are absorbed in the QCC than in the SQW structure, which is exactly the purpose of the QCC. Here, although the applied bias required to achieve maximum cooling power in the QCC is higher than the one required for the single QW structure, the COP at maximum J_Q is higher for the QCC (12.3 %) than for the SQW structure (9.3%).

The QCC shows an overall greater efficiency and greater CP than its single QW counterpart. There is, however, no significant reduction of the lattice temperature. This is due to the huge difference between the heat capacitance of electrons and phonons. In order to solve this problem, one would need to increase the amount of electrons in the QW regions. This could be achieved by heavily doping in the order of $10^{21\sim22}$ cm^{-3} or by considering metal/semiconductor junctions. This is however beyond the scope of the article.

IV. CONCLUSIONS

In the present work, we theoretically investigate the proposed Quantum Cascade Cooler device through the use of an in-house quantum code coupling heat and electron transport. We report anti-correlated electronic temperature oscillations as a function of voltage bias between two successive quantum wells. We show that such behaviour directly emerges from the possibility for electrons to absorb or emit polar optical phonons whose energy (35 meV) establishes the period of oscillations. Such bias dependence in the proposed heterostructure sheds light on the versatile physical properties which can emerge from this kind of device. The thermal properties of this device are also compared to its single quantum well counterpart. We show that the QCC leads to a significant improvement of both the

maximum cooling power and the efficiency, and is therefore a good candidate for solid state cooling upon optimization. The present QCC cooling structures may be also useful in devices in which electronic cooling plays an important role. Light-emitting devices will gain better efficiency if the carrier temperature can be decreased via our cooling device by 30–50 K. Non-radiative losses due to thermal escape of carriers outside the confining potential wells would be decreased. Similarly, in QW infrared photodetectors, the dark current will be reduced by cooling electrons in the QW. These are only a few examples. We believe there will be many more useful applications of electron cooling.

V. ACKNOWLEDGEMENT

This work was supported by the GELATO project from ANR (ANR-21-CE50-0017).

[1] A. Habibi Khalaj, T. Scherer, and S. K. Halgamuge, Energy, environmental and economical saving potential of data centers with various economizers across Australia, Applied Energy **183**, 1528 (2016).

[2] J. Ni and X. Bai, A review of air conditioning energy performance in data centers, Renewable and Sustainable Energy Reviews **67**, 625 (2017).

[3] B. Whitehead, D. Andrews, A. Shah, and G. Maidment, Assessing the environmental impact of data centres part 1: Background, energy use and metrics, Building and Environment **82**, 151 (2014).

[4] L. Xiu, Time Moore: Exploiting Moore's Law From The Perspective of Time, IEEE Solid-State Circuits Magazine **11**, 39 (2019).

[5] C. A. Mack, Fifty Years of Moore's Law, IEEE Transactions on Semiconductor Manufacturing **24**, 202 (2011).

[6] G. E. Moore, Lithography and the future of moore's law, IEEE Solid-State Circuits Society Newsletter **11**, 37 (2006).

[7] Q. Zhang, K. Deng, L. Wilkens, H. Reith, and K. Nielsch, Micro-thermoelectric devices, Nature Electronics **5**, 333 (2022).

[8] J. Mao, G. Chen, and Z. Ren, Thermoelectric cooling materials, Nature Materials **20**, 454 (2021).

[9] Y.-H. Gong, J. J. Yoo, and S. W. Chung, Thermal Modeling and Validation of a Real-World Mobile AP, IEEE Design & Test **35**, 55 (2018).

[10] C. Fiegna, Y. Yang, E. Sangiorgi, and A. G. O'Neill, Analysis of Self-Heating Effects in Ultrathin-Body SOI MOSFETs by Device Simulation, IEEE Transactions on Electron Devices **55**, 233 (2008).

[11] R. Gaska, A. Osinsky, J. Yang, and M. Shur, Self-heating in high-power AlGaN-GaN HFETs, IEEE Electron Device Letters **19**, 89 (1998).

[12] E. Pop, S. Sinha, and K. Goodson, Heat Generation and Transport in Nanometer-Scale Transistors, Proceedings of the IEEE **94**, 1587 (2006).

[13] K. M. Kretzschmar and D. R. Wilkie, The use of the Peltier effect for simple and accurate calibration of thermoelectric devices, Proceedings of the Royal Society of London. Series B. Biological Sciences **190**, 315 (1975).

[14] E. L. Murphy and R. H. Good, Thermionic Emission, Field Emission, and the Transition Region, Physical Review **102**, 1464 (1956).

[15] G. N. Hatsopoulos and E. P. Gyftopoulos, *Theory, technology, and application*, Thermionic energy conversion No. Vol. 2 (MIT Press, Cambridge, Mass, 1979).

[16] A. Yangui, M. Bescond, T. Yan, N. Nagai, and K. Hirakawa, Evaporative electron cooling in asymmetric double barrier semiconductor heterostructures, Nature Communications **10**, 4504 (2019).

[17] K. A. Chao, M. Larsson, and A. G. Mal'shukov, Room-temperature semiconductor heterostructure refrigeration, Applied Physics Letters **87**, 022103 (2005).

[18] J. Faist, F. Capasso, D. L. Sivco, C. Sirtori, A. L. Hutchinson, and A. Y. Cho, engQuantum cascade laser., Science (New York, N.Y.) **264**, 553 (1994), place: United States.

[19] M. Bescond, G. Dangoisse, X. Zhu, C. Salhani, and K. Hirakawa, Comprehensive Analysis of Electron Evaporative Cooling in Double-Barrier Semiconductor Heterostructures, Physical Review Applied **17**, 014001 (2022).

[20] J. Lai and A. Majumdar, Concurrent thermal and electrical modeling of sub-micrometer silicon devices, Journal of Applied Physics **79**, 7353 (1996).

[21] C. Jacoboni and L. Reggiani, The Monte Carlo method for the solution of charge transport in semiconductors with applications to covalent materials, Rev. Mod. Phys. **55**, 645 (1983), publisher: American Physical Society.

[22] S. Jin, Y. Park, and H. Min, A three-dimensional simulation of quantum transport in silicon nanowire transistor in the presence of electron-phonon interactions, Journal of Applied Physics **99**, 123719 (2006).

[23] M. Bescond, H. Carrillo-Nuñez, S. Berrada, N. Cavassilas, and M. Lannoo, Size and temperature dependence of the electron–phonon scattering by donors in nanowire transistors, Solid-State Electronics **122**, 1 (2016).

[24] M. Moussavou, M. Lannoo, N. Cavassilas, D. Logoteta, and M. Bescond, Physically based Diagonal Treatment of the Self-Energy of Polar Optical Phonons: Performance Assessment of III-V Double-Gate Transistors, Physical Review Applied **10**, 064023 (2018).

[25] A. Sood, J. A. Rowlette, C. G. Caneau, E. Bozorg-Grayeli, M. Asheghi, and K. E. Goodson, Thermal conduction in lattice–matched superlattices of InGaAs/InAlAs, Applied Physics Letters **105**, 051909 (2014).

[26] M. N. Luckyanova, J. A. Johnson, A. A. Maznev, J. Garg, A. Jandl, M. T. Bulsara, E. A. Fitzgerald, K. A. Nelson, and G. Chen, Anisotropy of the Thermal Conductivity in GaAs/AlAs Superlattices, Nano Letters **13**, 3973 (2013).

[27] E. Pop, R. Dutton, and K. Goodson, Detailed heat generation simulations via the monte carlo method, in *International Conference on Simulation of Semiconductor Processes and Devices, 2003. SISPAD 2003.* (2003) pp. 121–124.

[28] A. Shastry and C. A. Stafford, Temperature and voltage measurement in quantum systems far from equilibrium, Physical Review B **94**, 155433 (2016).

[29] C. A. Stafford, Local temperature of an interacting quantum system far from equilibrium, Physical Review B **93**, 245403 (2016).

[30] M. Lundstrom, *Fundamentals of Carrier Transport*, Cambridge books online (Cambridge University Press, 2000).

[31] M. Bescond and K. Hirakawa, High-Performance Thermionic Cooling Devices Based on Tilted-Barrier Semiconductor Heterostructures, Physical Review Applied **14**, 064022 (2020).